

Journal Name

Crossmark

PAPER

RECEIVED
dd Month yyyy
REVISED
dd Month yyyy

Stellarator island divertor shape optimization for reduced peak heat fluxes

Avigdor Veksler¹, Aaron Bader², Heinke Frerichs³, Elizabeth Paul¹¹Columbia University, New York NY, United States of America²Type One Energy, Knoxville TN, United States of America³University of Wisconsin — Madison, Madison WI, United States of America**E-mail:** av3249@columbia.edu**Keywords:** fusion plasma, optimization, island divertor

Abstract

An automated algorithm to construct island divertors for stellarators is presented and is used to find divertors that meet heat flux requirements determined by engineering and material limits. The algorithm uses just two initial conditions: two starting coordinates on the island separatrix. We leverage the simplicity of the algorithm to explore the divertor parameter space in a fixed magnetic equilibrium. Heat loads are approximated using the field line diffusion model implemented in the **FLARE** code. Optimal divertor solutions that satisfy engineering requirements are found using a parameter scan and a Bayesian optimization routine. The optimization achieves a 95% reduction in computational cost compared to the parameter scan. The resulting divertors are proven to be robust to varying plasma parameters through simulations with different cross-field heat diffusivities. This work represents a first step towards island divertor optimization for stellarators.

1 Introduction

The fusion community has experienced an influx of fusion power plant (FPP) designs, driven by advances in computational techniques and record-high investment in private fusion companies [1]. The stellarator community in particular has found advanced optimized equilibria [2, 3, 4], making the stellarator a lead FPP candidate design for private companies. As more suitable stellarator equilibria are found, the extrapolation of those equilibria to full-scale FPPs needs to be considered. This is typically where engineering and plant design meet the physics requirements of the FPP. One critical point of coordination between physics and engineering for stellarator FPPs is the power and particle exhaust solution. Fusion devices use a divertor to remove helium ash and other impurities. The divertor must also handle high heat fluxes from the incident thermal bulk plasma that is transported to the edge via collisional and turbulent processes.

One divertor solution for stellarators is the island divertor, which was first demonstrated in W7-AS [5] and has been extensively studied in the W7-X experiment [6, 7, 8, 9]. The island divertor relies on stellarator equilibria with a resonance in the rotational transform profile at the edge of the plasma. This opens up a large edge island chain. Metal plates are placed to cut through the island poloidally. Plasma transported to the edge will enter the island chain and travel through it until it impacts the divertor plates.

It is necessary for FPP divertors to be compatible with the intense heat fluxes coming from the incident plasma. Currently, materials used to construct divertors, such as tungsten, can only sustain maximum heat loads of 10 MW/m² before melting [10]. Exposure to heat loads greater than 10 MW/m² leads to cracking and recrystallization, which degrades the material's ability to withstand high thermal loads over time [11].

As such, it is ideal to reduce the peak heat loads on the divertor as much as possible. One benefit of stellarator island divertors is that the long connection lengths of stellarator islands help reduce the peak heat loads [12]. For stellarators, the target-to-target connection length measures the distance a field line travels from one surface before terminating on a second surface, such as a divertor plate [13]. These connection lengths determine the parallel transport time scales and hence the heat flux spread perpendicular to the magnetic field due to diffusive processes [13].

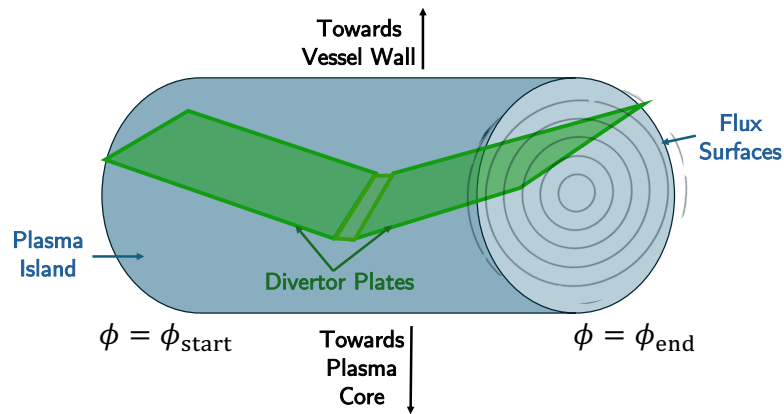


Figure 1. A cartoon of a V-shaped island divertor (green) in a stellarator island (blue cylinder, representative of a single stellarator island). Although in this cartoon the plates are shown to be planar, the ones created by the algorithm described in Fig. 2 allow for curved geometries in order to target the proper strike angle at both points of contact with the island separatrix. The divertor extends from $\phi = \phi_{\text{start}}$ to $\phi = \phi_{\text{end}}$, where ϕ is the toroidal angle of the stellarator in standard cylindrical coordinates. A rounded junction where the plates meet avoids having a sharp discontinuity in the divertor and is described more in Sec. 2.1.

Stellarator FPP solutions with planned island divertors should be designed with long connection lengths in the island region, since long connection lengths promote more perpendicular diffusion and lower peak heat loads on the divertor plates. Another way to reduce the peak heat loads is to shape the divertor plate with respect to the magnetic field geometry. Ensuring a small angle of incidence of the magnetic field to the divertor plate helps spread out the heat loads across the plate as much as possible.

There is previous work on divertor shape optimization. For tokamaks, adjoint-based methods were applied to optimize the shape of target plates using reduced edge physics models [14, 15], and recently, population-based methods, using field line diffusion models to estimate heat loads, were used to optimize divertor geometries [16]. For the stellarator island divertor, less optimization work has been performed. Previous research on W7-X explored the effect of magnetic geometry shaping with respect to the island divertor plate [17]. Work by Davies et al. [18] presents a semi-automated divertor generation algorithm to tilt divertor plates with respect to the magnetic field to reduce peak heat loads, but it does not search for an optimal divertor configuration.

The purpose of this work is to find the optimal divertor geometry to minimize its peak heat loads by exploring the divertor shaping with respect to a fixed background magnetic field equilibrium. The equilibrium used was presented in Hegna et al. [19]. Finding the optimal divertor is made possible by our fully-automated divertor design algorithm. We target reducing the peak heat loads as new computational capabilities in the FLARE code [20] make it possible to use this metric as part of an optimization loop. Other important physics, such as neutral transport, are not included in this analysis. Nevertheless, this work is a first step towards a comprehensive divertor design process that is necessary for full-device optimization [21].

In Sec. 2, the algorithm to automatically generate divertors is described, as well as the numerical simulation and cost function used to evaluate divertor performance. The divertors that result from the integration of the algorithm with a Bayesian optimization loop and their physics analysis are shown in Sec. 3. We conclude in Sec. 4.

2 Methods

The divertor-making algorithm described below creates an island divertor made up of straight segments at constant ϕ . The divertor geometry has curvature as these straight segments will vary in orientation as ϕ changes. In the toroidal direction, the divertor has a V-shape, where the tip of the V is closest to the core plasma. The rest of the divertor plates slope away from the core towards the confinement vessel wall. A cartoon image of this is shown in Fig. 1. This orientation is chosen to minimize divertor self-shadowing, which is an inefficient usage of the divertor plate, and to avoid creating local regions along the divertor only accessible to the plasma via cross-field transport, called target shadow regions [7].

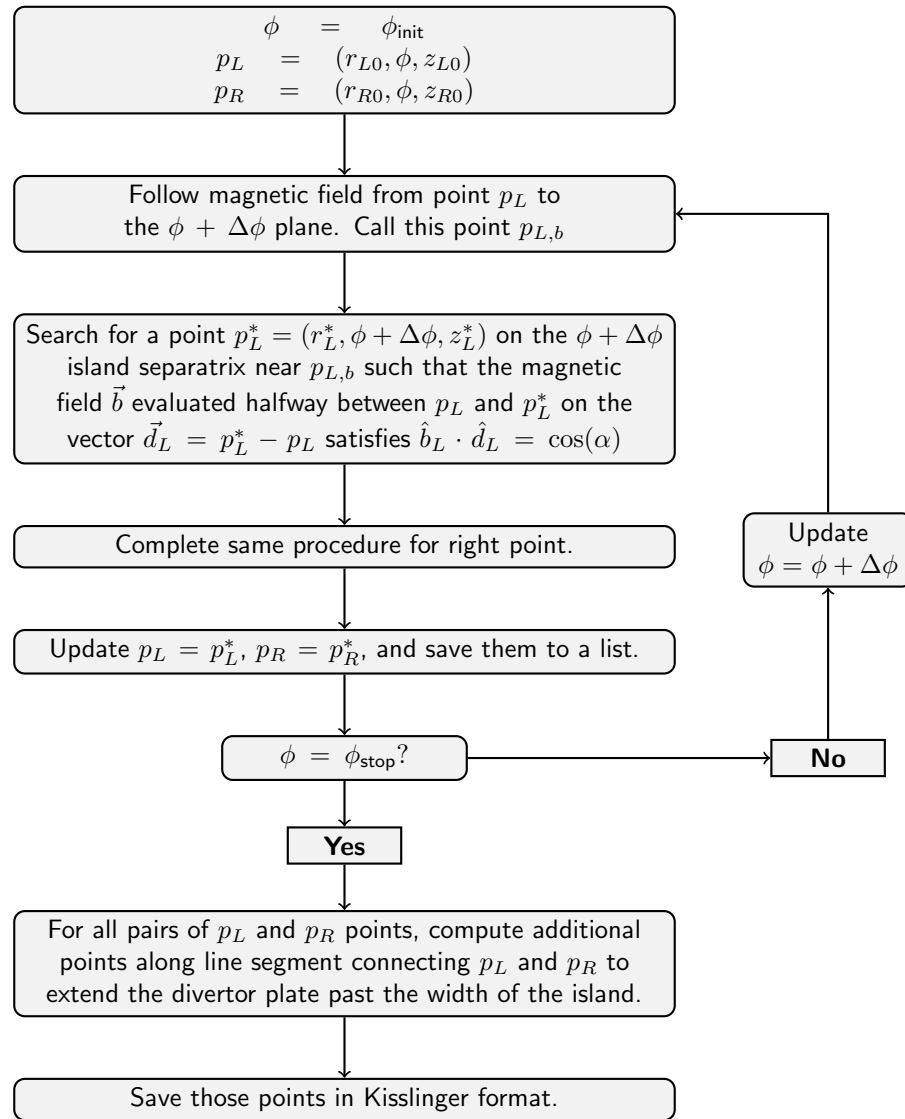


Figure 2. Algorithm that creates a divertor plate geometry from ϕ_{init} to ϕ_{end} . The algorithm is run with $\pm\Delta\phi$ to create a V-shaped divertor.

2.1 Divertor-making algorithm

In this section, we present a simple, low-dimensional parametrization of divertor construction. This algorithm creates divertors that aim to minimize the peak heat loads on the divertor by enforcing a maximum strike angle of the magnetic field on the divertor plates near the island separatrix. Maintaining a low strike angle helps spread the heat flux across the plate by increasing the area that is exposed to the plasma. We make no claim that the divertors are optimized with respect to other important considerations, such as neutrals or impurities.

The divertor-making algorithm is described in Fig. 2. The inputs required are: a discretization of points describing the island separatrix from ϕ_{start} to ϕ_{end} in increments of $\Delta\phi$, the capability to evaluate the plasma magnetic field beyond the LCFS, and two starting points on the island separatrix. In reality, a flux surface within the island near the island separatrix is used, called the control surface, as stochasticity of the separatrix would complicate the analysis. Only the control surface is used to construct the divertor. The rationale for this is that most of the heat flux will travel on flux tubes near the island separatrix towards the divertor plate [22]. The number of points describing the control surface per toroidal angle should be enough to be able to build a smooth periodic spline representation of the surface.

The output of the algorithm is two divertor plate files in Kisslinger format [13]. The files are text files that describe the geometry of divertor plates from $\phi \in [\phi_{\text{start}}, \phi_{\text{init}}]$ and from $\phi \in [\phi_{\text{init}}, \phi_{\text{end}}]$, where ϕ_{start} and ϕ_{end} are defined by the user. ϕ_{init} is the toroidal location of the tip of the V-shape. In this work, it was placed at the midpoint $\phi_{\text{init}} = (\phi_{\text{start}} + \phi_{\text{end}})/2$, but this does not have to be the case.

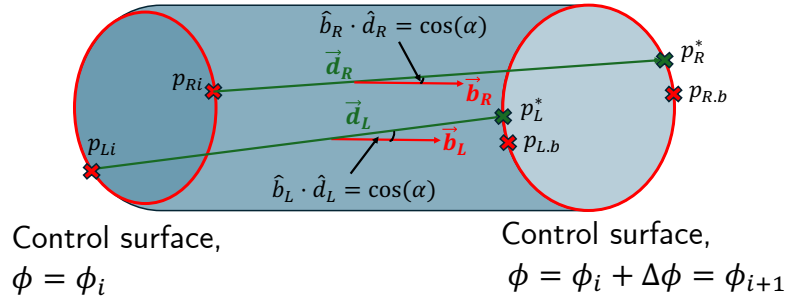


Figure 3. A visualization of how the coordinates of the divertor intersections with the control surface at different ϕ planes are chosen. The point p_L^* is found near the point $p_{L,b}$ such that $\hat{b}_L \cdot \hat{d}_L = \cos(\alpha)$. The same is repeated for the right points, and the divertor section between ϕ_i and ϕ_{i+1} is a surface going through $p_{Li}, p_L^*, p_{Ri}, p_R^*$.

The algorithm relies on two initial starting points on the control surface at $\phi = \phi_{\text{init}}$. From these two points, the rest of the divertor geometry is automatically generated. Let the initial starting points on the ϕ_{init} control surface be $p_{Li} = p_{L0} = (r_{L0}, \phi_{\text{init}}, z_{L0})$ and $p_{Ri} = p_{R0} = (r_{R0}, \phi_{\text{init}}, z_{R0})$ in a standard cylindrical coordinate system. The index i denotes the toroidal plane, starting from $i = 0$. We integrate the magnetic field trajectory from p_{Li} and p_{Ri} to the $\phi + \Delta\phi$ plane. These points also lie on the control surface, and call them $p_{L,b}$ and $p_{R,b}$. Now we search for points near $p_{L,b}$ and $p_{R,b}$ called p_L^* and p_R^* . We pick the points $p_j^*, j = L, R$ such that the magnetic field vector \vec{b}_j evaluated at $\vec{r}_j = \frac{1}{2}(\vec{p}_{ji} + \vec{p}_j^*)$ (the midpoint between p_{ji} and p_j^* along the vector $\vec{d}_j = \vec{p}_{ji} - \vec{p}_j^*$) satisfies $\hat{b}_j \cdot \hat{d}_j = \cos(\alpha)$, where α is the maximum strike angle specified for the divertor-making algorithm. A visualization of this process for the left point is shown in Fig. 3. The section of the divertor between ϕ and $\phi + \Delta\phi$ will be a surface going through p_{Li}, p_L^*, p_{Ri} , and p_R^* . This enforces that the magnetic field (and approximately, the incoming particle heat flux) would have a maximum strike angle of α with the divertor in the toroidal region ϕ to $\phi + \Delta\phi$.

The algorithm then steps toroidally in ϕ . The same procedure above is used but now from the $\phi + \Delta\phi$ plane, using $p_{j,i+1} = p_j^*$. This is repeated until we reach $\phi = \phi_{\text{stop}}$. The list of points $[p_{j0}, \dots, p_{jN}]$, where $N = |(\phi_{\text{init}} - \phi_{\text{stop}})|/\Delta\phi$, is saved. The algorithm is run twice, once where $\Delta\phi$ is positive and the stopping criterion $\phi_{\text{stop}} = \phi_{\text{end}}$ and once where $\Delta\phi$ is negative and the stopping criterion is $\phi_{\text{stop}} = \phi_{\text{start}}$. For every ϕ plane, additional points are used to extend the divertor plate along the line segment connecting p_L, p_R by $0.2 * |p_L - p_R|$. This ensures that the divertor captures the heat flux spreading in the region outside of the island.

At the end of the divertor-making algorithm, we create two additional divertor plate files. These are flat plates in the (r, z) plane that ensure no particles hit behind the divertor, and are described in more detail in Sec. 2.3

We choose $\phi_{\text{start}} = \pi/12$, $\phi_{\text{init}} = \pi/6$, $\phi_{\text{end}} = \pi/4$, and $\Delta\phi = \pi/360$. This means our divertor lies in a half-field period of the equilibrium magnetic field used in this work. This symmetry is exploited to reduce computational costs in Sec. 3. The strike angle α is also a user chosen parameter. For island divertors, it should be as low as possible, as it will enable spreading of the heat flux along the toroidal extent of the divertor. This helps minimize the peak heat flux on the divertor plate and stay within material heat flux limits. In this work the maximum strike angle was set to 3° . Although very small angles are a feature of current island divertors like in W7-X, there are risks to attempting to build divertors with such shallow angles in terms of engineering tolerances [23]. In principle, a minimum strike angle could be enforced with further adjustments of the divertor plate files.

In order to avoid a sharp discontinuity at ϕ_{init} where the two plates meet, the algorithm uses an input maximum strike angle α that increases linearly from 0.1° to 3° over the first four ϕ planes before and after ϕ_{init} . This creates a gradual slope where the two divertor plates meet.

The algorithm is a low-dimensional parametrization of divertor construction as there are only two inputs, the initial (p_{L0}, p_{R0}) starting points on the ϕ_{init} control surface. In practice the starting input coordinates are mapped to angles over a periodic B-spline representation of the control surface at ϕ_{init} . Thus, a pair of angles $(\theta_L, \theta_R) \in [0, 2\pi) \times [0, 2\pi)$ on the ϕ_{init} plane represent starting coordinates $p_L = (r_{L0}, \phi_{\text{init}}, z_{R0}), p_R = (r_{R0}, \phi_{\text{init}}, z_{R0})$, for the algorithm. The angles (θ_L, θ_R) represent a continuous, two dimensional input parameter space for the algorithm.

2.2 FLARE code

The FLARE [24] code is a magnetic meshing and field line analysis code, and is used to approximate heat flux loads on the divertors designed by the divertor-making algorithm. FLARE has an adaptive magnetic mesh generation algorithm [20]. The magnetic mesh consists of magnetic flux tubes which can quickly reconstruct field line positions using a local flux-tube coordinate system. The magnetic mesh is critical as it provides a significant speed up for field line tracing, around 100 - 1000 times faster [20] when compared to numerical integration of particle trajectories.

The other component of FLARE used is the field line tracing modules. Field line tracing can be used for simple models of heat flux transport. FLARE employs a field line diffusion model, which models heat transport via parallel streaming of particles along field lines and perpendicular diffusive kicks to model cross-field transport. Field line diffusion models are Monte-Carlo methods for the source-free continuity equation [13], solving

$$\vec{\nabla} \cdot (nC_s \vec{b} - D \vec{\nabla}_\perp n) = 0 \quad (1)$$

where n is the ion density, C_s is the ion sound speed, and D is a diffusion coefficient. In simulation, after a given parallel integration length $\Delta l = C_s \tau$ with timestep τ , the particles are kicked in the perpendicular direction by $\vec{\Delta}_\perp = \sqrt{4D\tau} \vec{\xi}_\perp$, where $\vec{\xi}_\perp$ is a randomly chosen unit vector perpendicular to the local magnetic field. Details on the implementation of the field line diffusion algorithm can be found in Frerichs et al. [20]. Proxies for heat loads on divertor plates can be estimated by initializing particles on the LCFS, and tracing their diffusive trajectories into the island and onto the divertor plates.

FLARE was used in this work to create a magnetic mesh for the equilibrium magnetic field and for field line diffusion approximations of heat loads on the divertor. Once the divertor plate files have been created by the divertor-making algorithm, they are passed to FLARE, which converts the plate files from Kisslinger format to a computational mesh. FLARE evaluates heat flux on the divertor by computing the intersection of field line trajectories on the magnetic mesh with the computational mesh of the divertor.

2.3 Evaluation of divertor performance

A metric is needed to compare the performance of different divertors produced by the divertor-making algorithm. We use a cost function for this purpose, as it will be used to guide optimization of divertors later on in Sec. 3.2. We use a relatively simple cost function that only targets the divertor performance with respect to heat flux, given by

$$J(\theta_L, \theta_R) = W_1 q_{\text{peak}} + W_2 \text{end-plate } \%, \quad (2)$$

where θ_L and θ_R are initial conditions for the divertor making algorithm, W_1 and W_2 are user determined weights, $q_{\text{peak}} = \max(q)$ is the maximum heat flux, and end-plate % measures how many field lines would hit undesirable positions in the divertor geometry. These undesirable positions are the initial leading edge of the divertor plate in the poloidal direction. To model this, we use additional divertor plate files that extend a fraction of a degree past ϕ_{start} and ϕ_{end} and create an end-plate extending radially away from the island towards the wall. Now, any field lines that would hit the finite-width edge of the divertor plate will register on the end-plate instead. The end-plate serves an additional purpose: to block field lines from hitting the divertor plate that enter the space between the divertor plates and the wall. These field lines would be registered the same as hits from the plasma facing side of the divertor, as we do not model the non-plasma facing components behind the divertor plates (i.e. pumps, cooling, support structure), and FLARE does not discriminate between field line hits on the front or backside of the divertor plate. As the end-plate measures field line hits to undesirable regions, we aim to minimize the percentage of field line strikes on the end-plate. This end-plate is only used as a computational boundary to help find good divertor solutions, and is not a part of the final divertor design.

The cost function combines both objectives of minimizing the peak heat flux and creating divertors viable from an engineering standpoint in that they are exposed to plasma only on the plasma facing component side.

3 Results

3.1 Divertor grid scan over starting angles

Since we have simplified the divertor-making algorithm to two parameters, we can visualize the entire parameter space with a contour plot. We employ a simple two-dimensional scan across the divertor parameter space. We create 441 pairs of starting angles by discretizing the range $[0, 2\pi)$

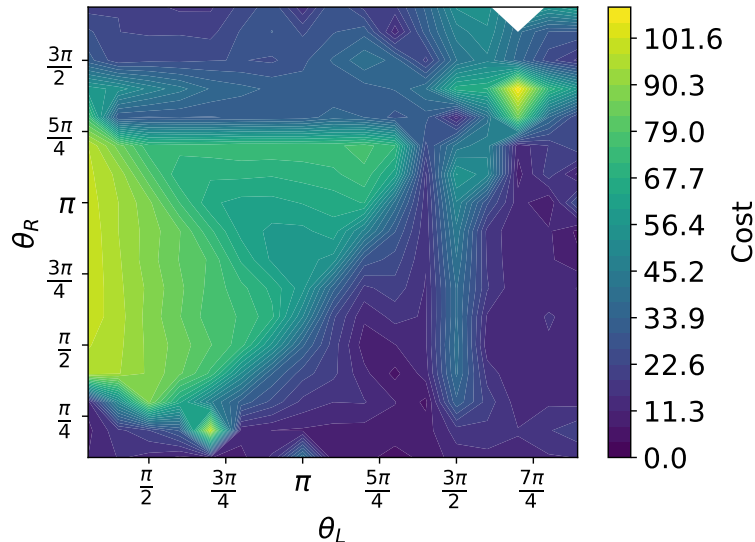


Figure 4. Cost function landscape for 441 divertors chosen from starting angles between 0 and 2π . The axes are scaled to capture the region of parameter space where the divertor-making algorithm completed successfully. The white area represents (θ_L, θ_R) initial conditions that did not produce a divertor because the divertor-making algorithm crashed.

with 21 points and choosing all combinations. Each set of angles (θ_L, θ_R) on the ϕ_{init} plane are used as initial conditions to create divertors. Heat loads are evaluated on every divertor using the `heat_load_proxy` task in `FLARE`, which performs a field line diffusion simulation. The results of the grid scan are shown in Fig. 4. The white area represents (θ_L, θ_R) initial conditions that did not produce a divertor because the divertor-making algorithm crashed. The reason for these crashes was that a numerical root-solve used to identify the point on the island spline for the correct strike angle could not converge. This is an uncommon occurrence and large regions of viable parameter space still exist. However, the cost function landscape does have areas of non-differentiability. In addition, it is non-convex. If more parameters were added to the divertor-making algorithm, the cost-function landscape would increase in dimensionality and complexity. The computational cost of such a scan is ~ 5 to 10 minutes per divertor using 128 cores on one Perlmutter AMD EPYC 7763 CPU node.

The lowest cost divertor from the grid scan has initial conditions $(\theta_L, \theta_R) = (4.08, 1.25)$, $q_{\text{peak}} = 2.915 \text{ MW/m}^2$, and an end-plate hit percentage of 3.487%.

3.2 Bayesian Optimization

Although the computational efficiency of `FLARE` is sufficient to run large grid scans and quickly evaluate a given divertor configuration with a reduced physics model, the computational expense is non-negligible, even with only two parameters to vary. Adding more degrees of freedom to the divertor-making algorithm would exacerbate this problem. We seek a computationally efficient way to search the algorithm parameter space and find a satisfactory divertor configuration. Ideally, we find the divertor that minimizes Eqn. 2. Bayesian optimization [25] is a popular optimization method for computationally expensive problems where gradients are not available. In our case, there are no numerical gradients using auto-differentiation given the statistical nature of `FLARE` simulations. Computing gradients using finite-differences is computationally prohibitive, and local, gradient-based methods would struggle and fail with the complexity and non-differentiability of the cost function landscape in Fig. 4. Bayesian optimization, on the other hand, is a global optimization method that may work well on these problems.

Bayesian optimization relies on statistical methods by assuming an underlying Gaussian process that models the cost function. This Gaussian process is assigned a covariance function, or kernel, which determines how observations in parameter space are correlated with each other. After making initial, random observations in parameter space, Bayesian optimization methods make their next observations based on an acquisition function. The acquisition function takes into account the mean of the Gaussian process and its standard deviation to balance exploration of parameter space and finding the optimal solution. On every step of the optimization, the Gaussian process is

updated, providing more information to make the next guess. After a few dozen iterations, the resulting Gaussian process can accurately model regions of parameter space and find the global optimum [26].

The open-source `BayesianOptimization` python package [27] is applied to the divertor shape optimization problem. The Gaussian process was set up to use a Matérn kernel [25], given by

$$k(x_i, x_j) = \frac{1}{\Gamma(\nu)2^{\nu-1}} \left(\frac{\sqrt{2\nu}}{l} d(x_i, x_j) \right)^\nu K_\nu \left(\frac{\sqrt{2\nu}}{l} d(x_i, x_j) \right),$$

where $d(\cdot, \cdot)$ is the Euclidean distance, $K_\nu(\cdot)$ is a modified Bessel function of order ν and $\Gamma(\cdot)$ is the gamma function. The parameter ν controls the smoothness of the kernel [28], and was set to 2.5. A soft barrier penalty of 200 is used to steer the model away from pairs of (θ_L, θ_R) that fail to produce a viable divertor. Because of this, the length scale of the Gaussian process is bounded between $0.1\times$ and $1.5\times$ the range of the domain in θ_L and θ_R . This ensures that the length scale does not collapse to near zero when imposing the soft penalty, which was noticed to be an issue in optimization. The optimizer uses an Expected Improvement [29] acquisition function equipped with a hyperparameter ξ that determines the relative weighting between exploitation and exploration of the cost function. This is in principle another hyperparameter that needs to be tuned. We tested ξ values of 0.005, 0.01, and 0.05. The best results were achieved using $\xi = 0.01$, and are presented below.

Fig. 5 shows the cost function landscape as learned by Bayesian optimization after 10 random initial exploration steps and 25 steps guided by the acquisition function. The majority of points are concentrated in the lower right corner, a valley in parameter space that is present in Fig. 4 as well. At this point in the optimization, we have already found a divertor that is near identical to the best one from the grid scan. The optimized divertor was found at $(\theta_L, \theta_R) = (4.05, 1.21)$, with $q_{\text{peak}} = 3 \text{ MW/m}^2$ and an end-plate hit percentage of 3.53%.

It is remarkable that the Bayesian optimization achieves practically the same result as the grid scan but with a 95% reduction in the number of divertors simulated. This result highlights the power of Bayesian approaches to expensive, black-box, and non-convex optimization problems. We expect that the savings would increase even more if the divertor-making algorithm parameter space was larger.

The optimizer does not exactly recreate the cost function landscape in Fig. 4, but there is no need to. The power in the optimization is to rapidly identify good regions of parameter space that should be further explored, either by further optimizations with a smaller domain, or more focused parameter grid scans. In the limit of many iterations, it is expected that the Bayesian optimizer would accurately recreate the cost function.

A concept useful in optimization is the Pareto frontier. The Pareto frontier represents the trade-off between constraints in an optimization problem. In our case, the trade off is the minimization of peak heat flux and ensuring that the plasma does not hit the end-plates. We vary the weight ratio of the two terms in the cost function, W_2/W_1 , and run an optimization with the cost function given by Eqn. 2 with the new weight ratio. We ran 100 optimizations with logarithmically spaced weight ratios from 10^{-2} to 10^2 . The resulting Pareto frontier formed by the lowest cost divertors in each case is shown in Fig. 6. Solutions along this Pareto frontier represent the best possible trade-off between q_{peak} and end-plate hit %. Fig. 6 shows that to get to end-plate %'s less than 5%, $q_{\text{peak}} \gtrsim 3 \text{ MW/m}^2$.

3.3 Heat Flux Profiles

In this section, we present the performance of the best optimized divertor in terms of the heat flux profiles on the divertor plate. The enforcement of a maximum strike angle is shown in Fig. 7. The heat flux profile for the divertor described in Sec. 3.2 is shown in Fig. 8. A 3D visualization is shown in Fig. 9. In Fig. 7 and Fig. 8, the white area represents regions with no divertor. The x-axis is parametrized in terms of distance from the plate center, as the divertor-making algorithm produces divertors that change width as the divertor plates move away from the core plasma further into the island.

One million particles are traced for every simulation. The ions in the plasma are set to have a density of $n_0 = 10^{19} \text{ m}^{-3}$, a temperature of 50 eV, and a cross field diffusion coefficient $\chi_\perp = 0.1 \text{ m}^2/\text{s}$. This value is justified by assuming that the perpendicular ion transport will be gyro-Bohm, and that $\chi \sim 1/B$ [30]. W7-X discharges have $B = 2.5 \text{ T}$. Meanwhile, the equilibrium used in this work has $B = 9 \text{ T}$. Thus, we expect χ to be reduced by a factor of 3.6. To connect back to χ_i , which is what is specified in FLARE, we use W7-X measurements of χ_e and the ratio

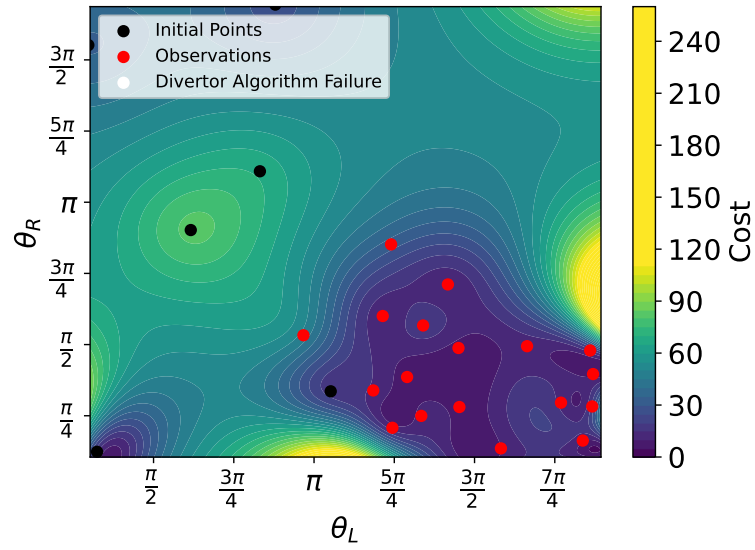


Figure 5. Cost function landscape as learned by a Bayesian optimization run. In black are the initial points used in the optimization, and in red the subsequent observations taken by the optimizer. The optimizer finds the large valley around $(\theta_L, \theta_R) = (4.5, 1.5)$.

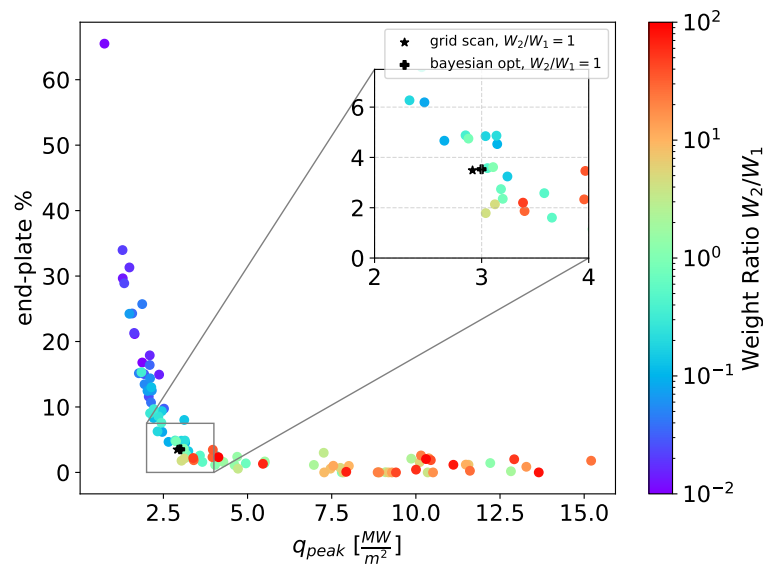


Figure 6. The Pareto frontier represents the best possible divertors when considering the trade off between the two terms in the cost function, q_{peak} and end-plate hit %. The results from the best divertors from the grid scan and the Bayesian optimization are also shown, and lie on the Pareto frontier.

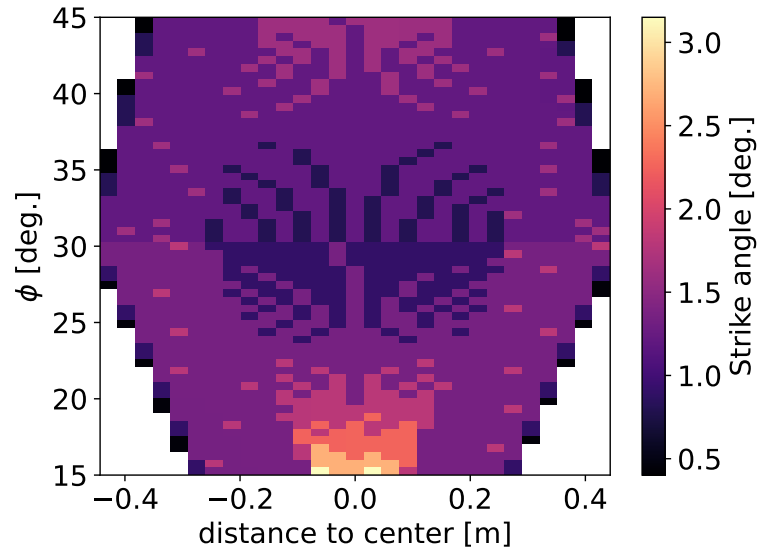


Figure 7. Strike angles on the divertor plate for a divertor created with $(\theta_L, \theta_R) = (4.05, 1.21)$. The strike angle is fairly uniform across the plate with a mean value of 1.56°.

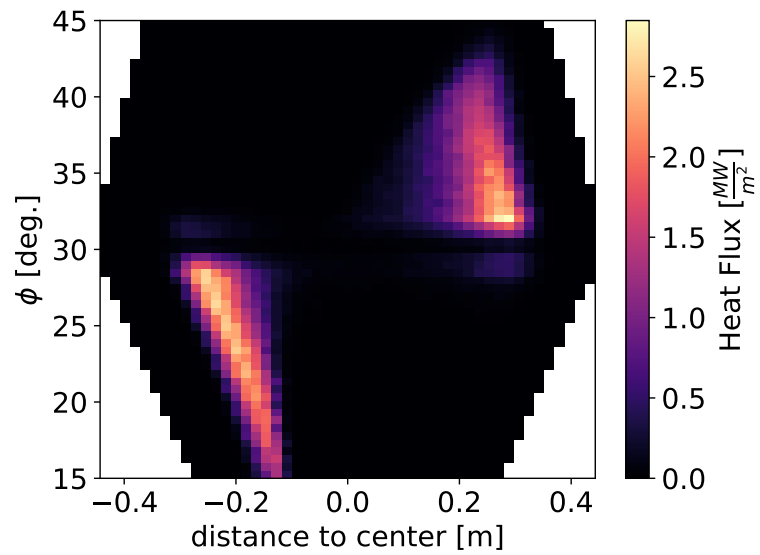


Figure 8. Heat flux q pattern on the divertor plate for a divertor created with $(\theta_L, \theta_R) = (4.05, 1.21)$. The black area represents the divertor computational domain. The peak heat flux is far below the 10 MW/m² limit.

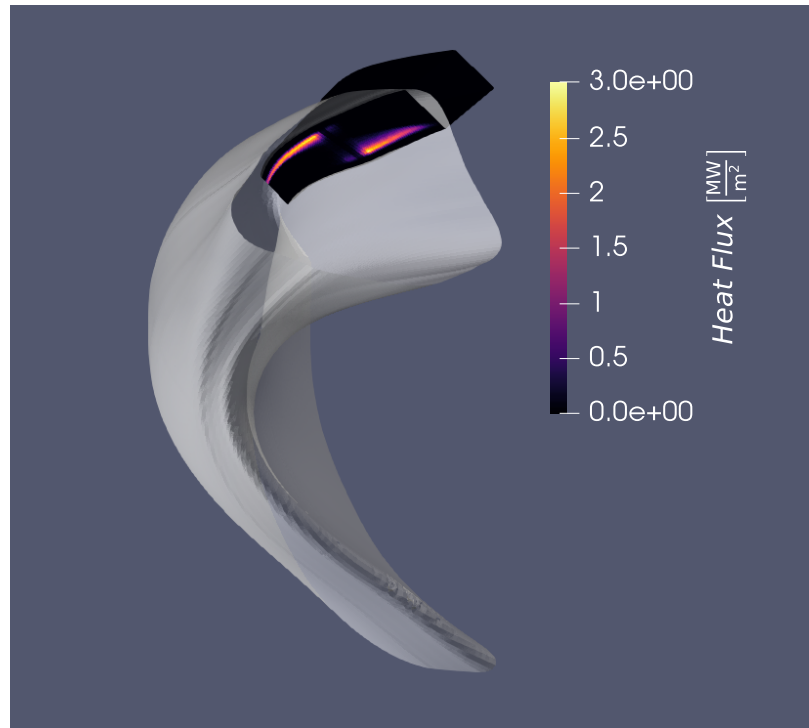


Figure 9. Heat flux q pattern on the divertor plate visualized in 3D. The vessel wall is shown in gray. The computational domain for the divertor is shown in black. The closing of the divertor structure past the domain of the vessel wall to avoid erroneous field line hits on the backside of the divertor can also be seen.

χ_e/χ_i . W7-X measurements report an edge $\chi_e \approx 0.5 \text{ m}^2/\text{s}$ [31]. Thus, in this equilibrium we can use $\chi_e \approx 0.5/3.6 = 0.13 \text{ m}^2/\text{s}$. Assuming $\chi_e/\chi_i \approx 1$ [32], our choice of $\chi_i = 0.1 \text{ m}^2/\text{s}$ is justified. It should be noted that this value is still a fairly conservative estimate. However, increasing it would simply increase the heat flux spread on the divertor plate and reduce q_{peak} . FLARE returns # particles hit/ m^2 across the computational domain. This is converted to a heat flux by multiplying by the assumed power entering the scrape-off-layer, which is assumed to be 8 MW [33].

3.4 Heat flux width scaling and divertor robustness

The optimization was performed with a single set of plasma parameters. However, a good divertor should ideally work across a range of plasma parameters, which may be seen, for example, in the transition from attachment to detachment [34], or during plasma start-up [35]. To test the robustness of the divertor to different plasma conditions, the artificial cross-field diffusion coefficient \mathcal{D} is varied for the optimized divertor shown in Fig. 9.

The measure of robustness used is the expected spreading of the heat-flux over the target plate. The heat flux width spread on the target divertor plate is denoted as $\lambda_{q,t}$. Assuming a scrape-off-layer with a constant L_c , the heat flux will spread out over a length scale of [13]

$$\lambda_{q,t} \sim \sqrt{\frac{DL_c}{C_s}}. \quad (3)$$

By keeping C_s fixed in the scan of diffusion coefficients, we expect $\lambda_{q,t} \sim \sqrt{\mathcal{D}}$. We measure $\lambda_{q,t}$ from simulation data following the procedure in Bader et al. [33]. For every toroidal angle of the divertor plate, we extract the 1D heat flux profile as a function of the distance to the center of the plate. To this distribution we fit a Gaussian distribution using `scipy.optimize.curve_fit`. A good proxy for $\lambda_{q,t}$ is an average over the toroidal angles of the full widths at half maximum (FWHM) of the heat flux profiles. The formula is given by

$$\lambda_{q,t} = \frac{1}{N} \sum_{i=1}^N (\text{FWHM})_i \frac{\max(q)_i}{\max(q)}, \quad (4)$$

where the index i represents the profiles at toroidal angle $\phi = \phi_{\text{init}} + i \times \Delta\phi$, and $N = |(\phi_{\text{init}} - \phi_{\text{stop}})|/\Delta\phi$. The scaling with respect to \mathcal{D} is shown in Fig. 10. Good agreement is seen for low diffusivities, but the scaling no longer agrees well for diffusivities above $3 \times 10^{-6} \text{ m}$.

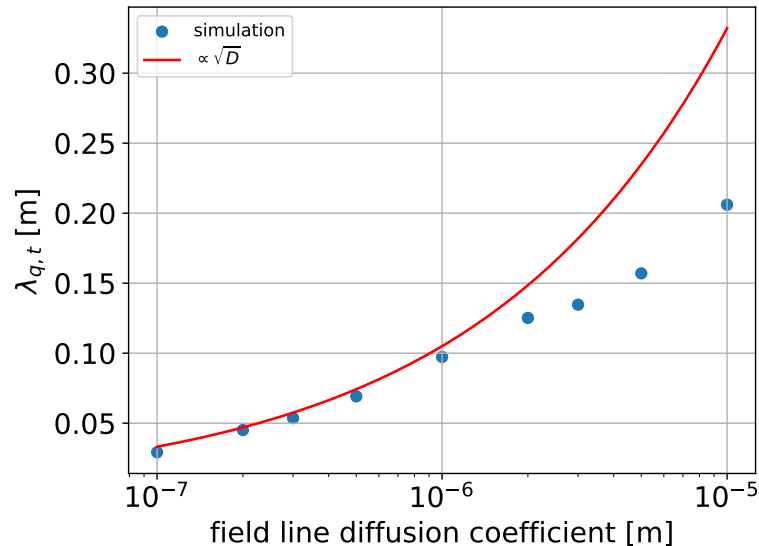


Figure 10. Scaling of $\lambda_{q,t}$ with respect to the cross-field diffusion coefficient. The scaling from Feng and W7-X-team [13] does not hold for high diffusivities as particles instead hit the vessel wall rather than the divertor plate.

The disagreement of the $\lambda_{q,t}$ scaling can be explained by looking at the percentage of particles that hit the vessel wall rather than the divertor plate, which increases with increasing diffusion coefficient. Having a significant fraction of particles striking the wall means that the divertor isn't capturing all the heat flux, and the scaling in Eqn. 3 no longer holds. In the set of simulations run in this work, we deviate from the scaling in Eqn. 3 once the wall hit percentage is above 5%.

4 Discussion and conclusions

This work presents an automated design and optimization of stellarator island divertors in fixed magnetic equilibria to help inform power exhaust solutions in stellarator FPPs. The optimization minimizes the peak heat flux incident on the divertor plate by changing the shape of the divertor with respect to the shape of the magnetic island boundary.

The optimization here is a proof-of-principle application to the boundary of FPPs, and there are many additions that can be made to support island divertor design for the stellarator community. First, this work only attempts to reduce the peak heat loads incident on the divertor plate. This work does not consider engineering constraints such as space for cooling and support structures, and manufacturing and alignment tolerances [36]. Future work should include terms in the cost function to better address these constraints. This applies as well to critical physics constraints that must be considered for any island divertor. Examples of this are maintaining a high neutral pressure, which is necessary for efficient pumping, but at the same time the neutrals should not backstream too much into the core. A similar consideration is the impurity transport and contamination of the core plasma.

There is also room to add complexity to the divertor-making algorithm. Some free parameters that were held fixed in this work but could be optimization parameters include the maximum strike angle α , the toroidal location of the divertor center ϕ_{init} , and the extent of the divertor with respect to the toroidal angle.

Eventually, divertor optimization tools should be integrated with the rest of the stellarator optimization suite. One could either evaluate the performance of equilibria with respect to a divertor using field line diffusion codes like FLARE within the optimization loop, or use it for post-processing analysis to validate potential equilibrium solutions.

Finally, divertor solutions optimized using field line diffusion models should be validated with higher fidelity codes, like EMC3-EIRENE [37]. EMC3-EIRENE has a more realistic plasma model, and takes into account neutral effects. However, these should not be used to replace field line diffusion models in the optimization loop due to their high computational cost.

Funding

This research was supported and funded by Type One Energy Group, Inc. © 2025 Type One Energy Group, Inc. All rights reserved. This research used resources of the National Energy

Research Scientific Computing Center (NERSC), a Department of Energy Office of Science User Facility using NERSC award ERCAP0031926.

References

- [1] Fusion Industry Association. The global fusion industry in 2024. Annual Report 4th Edition, Fusion Industry Association, July 2024. URL <https://www.fusionindustryassociation.org/wp-content/uploads/2024/07/2024-annual-global-fusion-industry-report.pdf>. Accessed: January 12, 2026.
- [2] Matt Landreman and Elizabeth Paul. Magnetic fields with precise quasisymmetry for plasma confinement. *Phys. Rev. Lett.*, 128:035001, Jan 2022. doi: 10.1103/PhysRevLett.128.035001. URL <https://link.aps.org/doi/10.1103/PhysRevLett.128.035001>.
- [3] A.G. Goodman, K. Camacho Mata, S.A. Henneberg, R. Jorge, M. Landreman, G.G. Plunk, H.M. Smith, R.J.J. Mackenbach, C.D. Beidler, and P. Helander. Constructing precisely quasi-isodynamic magnetic fields. *Journal of Plasma Physics*, 89(5):905890504, 2023. doi: 10.1017/S002237782300065X.
- [4] J. L. Velasco, I. Calvo, F. J. Escoto, E. Sánchez, H. Thienpondt, and F. I. Parra. Piecewise omnigenous stellarators. *Phys. Rev. Lett.*, 133:185101, Oct 2024. doi: 10.1103/PhysRevLett.133.185101. URL <https://link.aps.org/doi/10.1103/PhysRevLett.133.185101>.
- [5] P Grigull, K McCormick, J Baldzuhn, R Burhenn, R Brakel, H Ehmler, Y Feng, F Gadelmeier, L Giannone, D Hartmann, D Hildebrandt, M Hirsch, R Jaenicke, J Kisslinger, J Knauer, R König, G Kühner, H Laqua, D Naujoks, H Niedermeyer, N Ramasubramanian, N Rust, F Sardei, F Wagner, A Weller, U Wenzel, and the W7-AS Team. First island divertor experiments on the w7-as stellarator. *Plasma Physics and Controlled Fusion*, 43(12A):A175, nov 2001. doi: 10.1088/0741-3335/43/12A/313. URL <https://doi.org/10.1088/0741-3335/43/12A/313>.
- [6] T. Sunn Pedersen, R. König, M. Jakubowski, M. Krychowiak, D. Gradic, C. Killer, H. Niemann, T. Szepesi, U. Wenzel, A. Ali, G. Anda, J. Baldzuhn, T. Barbui, C. Biedermann, B.D. Blackwell, H.-S. Bosch, S. Bozhenkov, R. Brakel, S. Brezinsek, J. Cai, B. Cannas, J.W. Coenen, J. Cosfeld, A. Dinklage, T. Dittmar, P. Drewelow, P. Drews, D. Dunai, F. Effenberg, M. Endler, Y. Feng, J. Fellinger, O. Ford, H. Frerichs, G. Fuchert, Y. Gao, J. Geiger, A. Gorjaev, K. Hammond, J. Harris, D. Hathiramani, M. Henkel, Ye.O. Kazakov, A. Kirschner, A. Knieps, M. Kobayashi, G. Kocsis, P. Kornejew, T. Kremeyer, S. Lazerzon, A. LeViness, C. Li, Y. Li, Y. Liang, S. Liu, J. Lore, S. Masuzaki, V. Moncada, O. Neubauer, T.T. Ngo, J. Oelmann, M. Otte, V. Perseo, F. Pisano, A. Puig Sitjes, M. Rack, M. Rasinski, J. Romazanov, L. Rudischhauser, G. Schlisio, J.C. Schmitt, O. Schmitz, B. Schweer, S. Sereda, M. Slecicka, Y. Suzuki, M. Vecsei, E. Wang, T. Wauters, S. Wiesen, V. Winters, G.A. Wurden, D. Zhang, S. Zoletnik, and the W7-X. Team. First divertor physics studies in Wendelstein 7-X. *Nuclear Fusion*, 59(9):096014, July 2019. ISSN 0029-5515. doi: 10.1088/1741-4326/ab280f. URL <https://doi.org/10.1088/1741-4326/ab280f>. Publisher: IOP Publishing.
- [7] Y. Feng, M. Jakubowski, R. König, M. Krychowiak, M. Otte, F. Reimold, D. Reiter, O. Schmitz, D. Zhang, C.D. Beidler, C. Biedermann, S. Bozhenkov, K.J. Brunner, A. Dinklage, P. Drewelow, F. Effenberg, M. Endler, G. Fuchert, Y. Gao, J. Geiger, K.C. Hammond, P. Helander, C. Killer, J. Knauer, T. Kremeyer, E. Pasch, L. Rudischhauser, G. Schlisio, T. Sunn Pedersen, U. Wenzel, V. Winters, and W7-X. team. Understanding detachment of the W7-X island divertor. *Nuclear Fusion*, 61(8):086012, June 2021. ISSN 0029-5515. doi: 10.1088/1741-4326/ac0772. URL <https://doi.org/10.1088/1741-4326/ac0772>. Publisher: IOP Publishing.
- [8] Y. Feng, Y. Gao, T. Kremeyer, D. Gradic, L. Rudischhauser, G. Fuchert, S. Bozhenkov, M. Endler, M. Jakubowski, R. Koenig, M. Krychowiak, E. Pasch, K.C. Hammond, and W7-X. Team. First attempt to quantify W7-X island divertor plasma by local experiment-model comparison. *Nuclear Fusion*, 61(10):106018, September 2021. ISSN 0029-5515. doi: 10.1088/1741-4326/ac2025. URL <https://doi.org/10.1088/1741-4326/ac2025>. Publisher: IOP Publishing.

- [9] K C Hammond, Y Gao, M Jakubowski, C Killer, H Niemann, L Rudischhauser, A Ali, T Andreeva, B D Blackwell, K J Brunner, B Cannas, P Drewelow, P Drews, M Endler, Y Feng, J Geiger, O Grulke, J Knauer, S Klose, S Lazerson, M Otte, F Pisano, U Neuner, A Puig Sitjes, K Rahbarnia, J Schilling, H Thomsen, G A Wurden, and the W7-X. team. Drift effects on W7-X divertor heat and particle fluxes. *Plasma Physics and Controlled Fusion*, 61(12):125001, October 2019. ISSN 0741-3335. doi: 10.1088/1361-6587/ab4825. URL <https://doi.org/10.1088/1361-6587/ab4825>. Publisher: IOP Publishing.
- [10] F. Escourbiac, A. Durocher, A. Fedosov, T. Hirai, R.A. Pitts, P. Gavila, B. Riccardi, V. Kuznetsov, A. Volodin, and A. Komarov. Assessment of critical heat flux margins on tungsten monoblocks of the iter divertor vertical targets. *Fusion Engineering and Design*, 146:2036–2039, 2019. ISSN 0920-3796. doi: <https://doi.org/10.1016/j.fusengdes.2019.03.094>. URL <https://www.sciencedirect.com/science/article/pii/S0920379619304168>. SI:SOFT-30.
- [11] Yu-Zhong Jin, Xiang Liu, You-Yun Lian, and Jiu-Peng Song. Influence of recrystallization on tungsten divertor monoblock under high heat flux. *Tungsten*, 4(3):194–202, September 2022. ISSN 2661-8036. doi: 10.1007/s42864-021-00126-1. URL <https://doi.org/10.1007/s42864-021-00126-1>.
- [12] Y Feng, M Kobayashi, T Lunt, and D Reiter. Comparison between stellarator and tokamak divertor transport. *Plasma Physics and Controlled Fusion*, 53(2):024009, January 2011. ISSN 0741-3335. doi: 10.1088/0741-3335/53/2/024009. URL <https://dx.doi.org/10.1088/0741-3335/53/2/024009>.
- [13] Y Feng and W7-X-team. Review of magnetic islands from the divertor perspective and a simplified heat transport model for the island divertor. *Plasma Physics and Controlled Fusion*, 64(12):125012, November 2022. ISSN 0741-3335. doi: 10.1088/1361-6587/ac9ed9. URL <https://dx.doi.org/10.1088/1361-6587/ac9ed9>. Publisher: IOP Publishing.
- [14] W. Dekeyser, D. Reiter, and M. Baelmans. Divertor target shape optimization in realistic edge plasma geometry. *Nuclear Fusion*, 54(7):073022, May 2014. ISSN 0029-5515. doi: 10.1088/0029-5515/54/7/073022. URL <https://doi.org/10.1088/0029-5515/54/7/073022>. Publisher: IOP Publishing.
- [15] M. Baelmans, M. Blommaert, W. Dekeyser, and T. Van Oevelen. Achievements and challenges in automated parameter, shape and topology optimization for divertor design. *Nuclear Fusion*, 57(3):036022, January 2017. ISSN 0029-5515. doi: 10.1088/1741-4326/57/3/036022. URL <https://doi.org/10.1088/1741-4326/57/3/036022>. Publisher: IOP Publishing.
- [16] H. Frerichs. Particle swarm optimization of divertor targets for heat load control, August 2025. URL <http://arxiv.org/abs/2509.00206>. arXiv:2509.00206 [physics].
- [17] Thomas Sunn Pedersen, Ralf König, Maciej Krychowiak, Marcin Jakubowski, Jürgen Baldzuhn, Sergey Bozhenkov, Golo Fuchert, Andreas Langenberg, Holger Niemann, Daihong Zhang, Kian Rahbarnia, Hans-Stephan Bosch, Yevgen Kazakov, Sebastijan Brezinsek, Yu Gao, Novimir Pablant, and the W7-X. Team. First results from divertor operation in Wendelstein 7-X. *Plasma Physics and Controlled Fusion*, 61(1):014035, November 2018. ISSN 0741-3335. doi: 10.1088/1361-6587/aaec25. URL <https://doi.org/10.1088/1361-6587/aaec25>. Publisher: IOP Publishing.
- [18] Robert Davies, Yuhe Feng, Dieter Boeyaert, John C. Schmitt, Michael J. Gerard, Kelly A. Garcia, Oliver Schmitz, Benedikt Geiger, and Sophia A. Henneberg. A semi-automated algorithm for designing stellarator divertor and limiter plates and application to HSX. *Nuclear Fusion*, 64(12):126044, October 2024. ISSN 0029-5515. doi: 10.1088/1741-4326/ad8017. URL <https://doi.org/10.1088/1741-4326/ad8017>. Publisher: IOP Publishing.
- [19] C.C. Hegna, D.T. Anderson, E.C. Andrew, A. Ayilaran, A. Bader, T.D. Bohm, K. Camacho Mata, J.M. Canik, L. Carbajal, A. Cerfon, and et al. The infinity two fusion pilot plant baseline plasma physics design. *Journal of Plasma Physics*, 91(3):E76, March 2025. doi: 10.1017/S0022377825000364.
- [20] H Frerichs, D Boeyaert, Y Feng, and K A Garcia. Magnetic mesh generation and field line reconstruction for scrape-off layer and divertor modeling in stellarators. *Plasma Physics and Controlled Fusion*, 67(4):045012, March 2025. ISSN 0741-3335. doi:

- 10.1088/1361-6587/adbb8c. URL <https://dx.doi.org/10.1088/1361-6587/adbb8c>. Publisher: IOP Publishing.
- [21] D.A. Gates, A.H. Boozer, T. Brown, J. Breslau, D. Curreli, M. Landreman, S.A. Lazerson, J. Lore, H. Mynick, G.H. Neilson, N. Pomphrey, P. Xanthopoulos, and A. Zolfaghari. Recent advances in stellarator optimization. *Nuclear Fusion*, 57(12):126064, October 2017. ISSN 0029-5515. doi: 10.1088/1741-4326/aa8ba0. URL <https://dx.doi.org/10.1088/1741-4326/aa8ba0>. Publisher: IOP Publishing.
- [22] F. Effenberg, H. Niemann, Y. Feng, J. Geiger, O. Schmitz, Y. Suzuki, A. Ali, T. Barbui, S. Brezinsek, H. Frerichs, M. Jakubowski, R. König, M. Krychowiak, A. Puig Sitjes, J. C. Schmitt, and T. Sunn Pedersen. Investigation of 3D effects on heat fluxes in performance-optimized island divertor configurations at Wendelstein 7-X. *Nuclear Materials and Energy*, 18:262–267, 2019. ISSN 2352-1791. doi: <https://doi.org/10.1016/j.nme.2019.01.006>. URL <https://www.sciencedirect.com/science/article/pii/S2352179118302394>.
- [23] Josiah T. Wai. *Shape and Divertor Control in Tokamaks*. PhD thesis, Princeton University, 2023. Copyright - Database copyright ProQuest LLC; ProQuest does not claim copyright in the individual underlying works; Last updated - 2025-02-03.
- [24] H. Frerichs. FLARE: field line analysis and reconstruction for 3D boundary plasma modeling. *Nuclear Fusion*, 64(10):106034, September 2024. ISSN 0029-5515. doi: 10.1088/1741-4326/ad7303. URL <https://dx.doi.org/10.1088/1741-4326/ad7303>. Publisher: IOP Publishing.
- [25] Peter I. Frazier. *Bayesian Optimization*, chapter 11, pages 255–278. Institute for Operations Research and the Management Sciences, 2018. doi: 10.1287/educ.2018.0188. URL <https://pubsonline.informs.org/doi/abs/10.1287/educ.2018.0188>.
- [26] Donald R. Jones, Matthias Schonlau, and William J. Welch. Efficient Global Optimization of Expensive Black-Box Functions. *Journal of Global Optimization*, 13(4):455–492, December 1998. ISSN 1573-2916. doi: 10.1023/A:1008306431147. URL <https://doi.org/10.1023/A:1008306431147>.
- [27] Fernando Nogueira. Bayesian optimization: Open source constrained global optimization tool for python, 2014, 2020.
- [28] Carl Edward Rasmussen and Hannes Nickisch. Gaussian processes for machine learning (gpml) toolbox. *J. Mach. Learn. Res.*, 11:3011–3015, December 2010. ISSN 1532-4435.
- [29] Dawei Zhan and Huanlai Xing. Expected improvement for expensive optimization: a review. *Journal of Global Optimization*, 78(3):507–544, November 2020. ISSN 1573-2916. doi: 10.1007/s10898-020-00923-x. URL <https://doi.org/10.1007/s10898-020-00923-x>.
- [30] G. Manfredi and M. Ottaviani. Gyro-bohm scaling of ion thermal transport from global numerical simulations of ion-temperature-gradient-driven turbulence. *Phys. Rev. Lett.*, 79: 4190–4193, Nov 1997. doi: 10.1103/PhysRevLett.79.4190. URL <https://link.aps.org/doi/10.1103/PhysRevLett.79.4190>.
- [31] G.M. Weir, P. Xanthopoulos, M. Hirsch, U. Höfel, T. Stange, N. Pablant, O. Grulke, S. Äkäslompolo, J. Alcusón, S. Bozhenkov, M. Beurskens, A. Dinklage, G. Fuchert, J. Geiger, M. Landreman, A. Langenberg, S. Lazerson, N. Marushchenko, E. Pasch, J. Schilling, E.R. Scott, Y. Turkin, T. Klinger, and the W7-X. Team. Heat pulse propagation and anomalous electron heat transport measurements on the optimized stellarator W7-X. *Nuclear Fusion*, 61(5):056001, March 2021. ISSN 0029-5515. doi: 10.1088/1741-4326/abea55. URL <https://doi.org/10.1088/1741-4326/abea55>. Publisher: IOP Publishing.
- [32] M Wappl, S A Bozhenkov, T Andreeva, S Bannmann, H M Smith, R C Wolf, and the W7-X. Team. Experimental power balance study on turbulent heat transport at Wendelstein 7-X. *Plasma Physics and Controlled Fusion*, 67(7):075025, July 2025. ISSN 0741-3335. doi: 10.1088/1361-6587/ade824. URL <https://doi.org/10.1088/1361-6587/ade824>. Publisher: IOP Publishing.

- [33] A. Bader, A. Ayilaran, J.M. Canik, A. De, W. Guttenfelder, C.C. Hegna, M. Knilans, A. Malkus, T.S. Pedersen, P. Sinha, J. Talley, D. Velez, K. Willis, and Type One Energy Group. Power and particle exhaust for the Infinity Two fusion pilot plant. *Journal of Plasma Physics*, 91(2):E67, April 2025. ISSN 0022-3778, 1469-7807. doi: 10.1017/S0022377825000273. URL https://www.cambridge.org/core/product/identifier/S0022377825000273/type/journal_article.
- [34] B. J. Peterson, G. Partesotti, F. Reimold, G. A. Wurden, Y. Gao, D. Zhang, V. Winters, M. Kobayashi, Y. Feng, K. Mukai, and J. von Miller. Investigation of island size effect on radiation distribution during attached and detached plasmas in the island divertor of W7-X. *Nuclear Materials and Energy*, 42:101868, March 2025. ISSN 2352-1791. doi: 10.1016/j.nme.2025.101868. URL <https://www.sciencedirect.com/science/article/pii/S2352179125000080>.
- [35] S. Zhou, Y. Liang, A. Knieps, Y. Suzuki, J. Geiger, A. Dinklage, A. Langenberg, E. Pasch, M. Jakubowski, N. Pablant, N.C. Wang, P. Drews, S. Bozhenkov, S. Liu, S. Xu, Y. Gao, Y.H. Ding, Z. Huang, and the W7-X. Team. Equilibrium effects on the structure of island divertor and its impact on the divertor heat flux distribution in Wendelstein 7-X. *Nuclear Fusion*, 62(10):106002, August 2022. ISSN 0029-5515. doi: 10.1088/1741-4326/ac8439. URL <https://doi.org/10.1088/1741-4326/ac8439>. Publisher: IOP Publishing.
- [36] Jeremy D. Lore, Tamara Andreeva, Jean Boscary, Sergey Bozhenkov, Joachim Geiger, Jeffrey H. Harris, Hauke Hoelbe, Arnold Lumsdaine, Dean McGinnis, Alan Peacock, and Joseph Tipton. Design and analysis of divertor scraper elements for the w7-x stellarator. *IEEE Transactions on Plasma Science*, 42(3):539–544, 2014. doi: 10.1109/TPS.2014.2303649.
- [37] Y. Feng, H. Frerichs, M. Kobayashi, A. Bader, F. Effenberg, D. Harting, H. Hoelbe, J. Huang, G. Kawamura, J. D. Lore, T. Lunt, D. Reiter, O. Schmitz, and D. Sharma. Recent improvements in the emc3-eirene code. *Contributions to Plasma Physics*, 54(4-6):426–431, 2014. doi: <https://doi.org/10.1002/ctpp.201410092>. URL <https://onlinelibrary.wiley.com/doi/abs/10.1002/ctpp.201410092>.